Check for updates

View Article Online
View Journal

Journal of
Materials Chemistry C
Materials for optical, magnetic and electronic devices

Accepted Manuscript

This article can be cited before page numbers have been issued, to do this please use: P. Gonzalez-Izquierdo, O. Fabelo, L. Canadillas-Delgado, G. Beobide, O. Vallcorba, M. Sánchez-Andújar, M. T. Fernandez-Diaz and M. de Pedro, *J. Mater. Chem. C*, 2020, DOI: 10.1039/D0TC02341H.

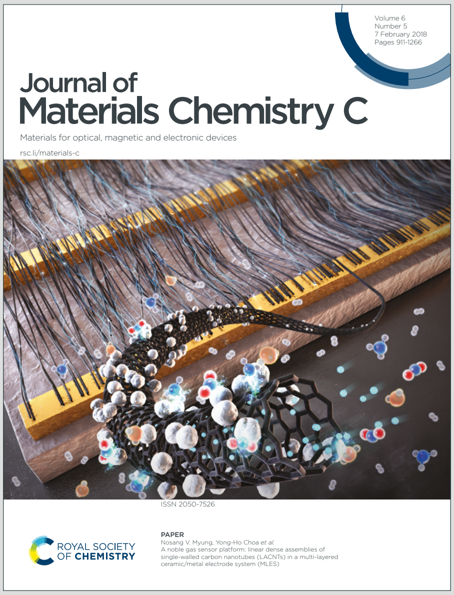

Volume 6
Number 5
7 February 2018
Pages 911-1266

Journal of
Materials Chemistry C
Materials for optical, magnetic and electronic devices
rsc.li/materials-c

ISSN 2050-7526

ROYAL SOCIETY
OF CHEMISTRY

PAPER
Nosang V. Myung, Yong-Ho Choa *et al.*
A noble gas sensor platform: linear dense assemblies of single-walled carbon nanotubes (LACNTs) in a multi-layered ceramic/metal electrode system (MLES)

This is an Accepted Manuscript, which has been through the Royal Society of Chemistry peer review process and has been accepted for publication.

Accepted Manuscripts are published online shortly after acceptance, before technical editing, formatting and proof reading. Using this free service, authors can make their results available to the community, in citable form, before we publish the edited article. We will replace this Accepted Manuscript with the edited and formatted Advance Article as soon as it is available.

You can find more information about Accepted Manuscripts in the Information for Authors.

Please note that technical editing may introduce minor changes to the text and/or graphics, which may alter content. The journal's standard Terms & Conditions and the Ethical guidelines still apply. In no event shall the Royal Society of Chemistry be held responsible for any errors or omissions in this Accepted Manuscript or any consequences arising from the use of any information it contains.

ROYAL SOCIETY
OF CHEMISTRY

rsc.li/materials-c

View Article Online
DOI: 10.1039/D0TC02341H

Temperature Evolution of (quinuclidinium)[FeCl$_4$]; a Plastic/Polar Magnetic Hybrid Compound with Giant Dielectric Constant

Palmerina González-Izquierdo,[a,b] Oscar Fabelo,*[b] Laura Canadillas-Delgado,[b] Garikoitz Beobide,[c,d] Oriol Vallcorba,[e] Manuel Sánchez-Andújar,[f] María Teresa Fernández-Díaz[b] and Imanol de Pedro*[a]*

[a] CITIMAC, Facultad de Ciencias, Universidad de Cantabria, 39005 Santander.

[b] Institut Laue-Langevin, BP 156X, F-38042 Grenoble Cedex, France.

[c] Departamento de Química Inorgánica, Facultad de Ciencia y Tecnología, Universidad del País Vasco, Apartado 644, E-48080, Bilbao, Spain.

[d] Basque Ctr Mat Applicat & Nanostruct, BCMat, UPV EHU Sci Pk, Leioa 48940, Spain.

[e] ALBA Synchrotron Light Source, Cerdanyola del Vallés, Barcelona, Spain.

[f] QuiMolMat Group, Department of Chemistry, Faculty of Science and Advanced Scientific Research Center (CICA), Zapateira, University of A Coruna, 15071 A Coruna, Spain.

Keywords: Hybrid compounds; Crystal and Magnetic Structure; Halometallate Complexes; Magneto-Structural Correlations; Long-range Magnetic Ordering, Ferroelectric, Plastic Crystals.

ABSTRACT

The temperature evolution of the physical properties of the (quinuclidinium)[FeCl$_4$] compound shows an unprecedented series of phase, structural and magnetic transitions. Above 390 K, a plastic phase (or also termed as ‘‘rotator phases’’) is observed (phase **I**). Between 390 K and 280 K, an intermediate phase solved in a non-centrosymmetric space group has been characterized. The crystallographic studies show that the compound crystallizes on the $Pbc2_1$ polar space group (phase **II**), and therefore the phase transition between **I** and **II** involves a paraelectric-to-polar phase transition. This result is confirmed through complex dielectric permittivity. Moreover, the real part of the dielectric permittivity presents a giant increase above 390 K, reaching a maxima of 10^5 value that is notably larger than any other hybrid compound previously reported. Below 280 K a third structural phase transition is observed, that involves the doubling of the unit cell and a change of symmetry due to the blocking of the counter-ions. The phase **III** crystallizing in the $Pbca$ centrosymmetric space group. Below 3.5 K, long-range magnetic order is detected. Neutron diffraction below the order temperature suggests a breaking of symmetry and the magnetic structure in phase **IV** was solved in the $P2_1'2_1'2_1$ Shubnikov space group, giving rises to a ferrimagnetic structure that allows a net ferromagnetic signal along the c-axis.

View Article Online
DOI: 10.1039/D0TC02341H

1. Introduction

Hybrid organic-inorganic crystals are unique materials that have been attracting increasing interest in the last years due to their physical properties and potential applications in different fields, as photovoltaic, [1-7]lithium batteries,[8] photomechanic materials,[9] between others. Among these applications, the development of high conductivity solid state electrolytes for fuel cells, batteries and solar cells is one of the most explored areas,[10-11] in comparison with the polymers electrolytes that generally show low conductivity.[12-13] In that sense, they are comparable with the classic ceramic conductors, such as doped lithium titanium phosphate, that allows fast ion transport.[14-15] However, these materials present the considerable disadvantage of their fragility and, in some cases, an important toxicity. In order to overcome this problem, a new type of materials has been proposed: the plastic hybrid materials. Although plastic crystals were described in the 60's,[16] there is no rule to predict which cation and anion combinations will yield plastic crystalline materials and which will form salts that melt before any rotator phase is achieved. It deserves to be noted that a plastic crystal has long-range structural order but short-range disorder, which is typically due to the occurrence of rotational motions of the constituents.[17-21] This plastic phase can be seen as a mesophase between the solid and liquid phases that is often found in molecules with globular structures. That means, they are symmetrical around their center (CH_4,CCl_4, NH_4 pentaerythritol, etc.); or they give a sphere by rotation around an axis (cyclohexane, camphor, etc.). [16, 22] The combination of two or more units to form hybrid materials can be desirable to enhance the multifunctionality of the system, for example doping the plastic crystalline phases with a lithium imide salt to be utilized as solid electrolytes for lithium batteries.[23-26] An alternative is to combine the physical properties by tuning the different constituents: ferroelectricity from the polar molecule and long-range magnetic order from magnetic anions.

A recently discovered plastic/ferroelectric hybrid molecular crystal, (quinuclidinium)[ReO_4] (quinuclidine = 1-azabicyclo[2.2.2]octane), which presents a plastic crystal phase at high temperature, a paraelectric phase and a ferroelectric phase at low temperature, has been reported.[27] This system exhibits ferroelectricity above room temperature (RT) and undergoes a phase transition to a plastic crystal phase at a higher temperature (367 K). The phase transition between ferroelectric and plastic phases involves changes of the crystal lattice symmetry, from hexagonal and cubic, which allowed an easy modification of the crystal orientation and the direction of the polarization axis by the application of an external electric field. Similar results were reported for quinuclidinium periodate.[28] Recently, two new compounds synthetized with 1-Azabicyclo[2.2.1]heptanium molecule and periodate or perrhenate were reported with similar plastic/ferroelectric phase transiton.[29] These studies show that the combination of a globular cation with a tetrahedral anion results in the formation of plastic crystals. Moreover, these systems present ferroelectricity in a low temperature phase, when at least one of the ions possesses an electric dipole, as it is the case of the quinuclidine molecule.

Motivate for these works, in this paper, we explore the temperature evolution of a new complex of formula (quinuclidinium)[$FeCl_4$] (chemical structural formula $C_7H_{14}NFeCl_4$). The inclusion

View Article Online
DOI: 10.1039/D0TC02341H

of $[FeCl_4]^-$ anion gives rises to long-range magnetic order at low temperature. Moreover, due to the high flexibility of this hybrid compound, a series of structural phase transitions were also observed reaching a plastic/paraelectric phase above 390 K. Below the plastic phase, the (quinuclidinium)$[FeCl_4]$ compound crystallizes in the $Pbc2_1$ non-centrosymmetric (polar) space group, therefore ferroelectricity is allowed by symmetry. This intermediate polar phase is stable between 390 K and 280 K. Below this temperature, the libration of the quinuclidinium molecule is decreasing and a second phase transition is observed. This new phase crystallizes in the *Pbca* centrosymmetric space group and it is stable up to the occurrence of the long-range magnetic order at ca. 3 K. The magnetic structure was determined at 1.4 K in the $P2_1'2_1'2_1$ Shubnikov space group. A scheme of the different phases respect to the temperature is presented in Table 1. Single crystal diffraction and powder diffraction using neutrons, laboratory X-ray and synchrotron diffraction techniques have been used to characterize the different structural and magnetic phases. Macroscopic measurements were also carried out to follow the temperature dependence of the real part of the complex dielectric permittivity from RT to 430 K. The magnetic susceptibility was also studied from RT to 2 K. Here below all these results will be discussed in detail.

Table 1 Scheme of the different phase transitions of the title compound.

470 → 390 K **I** $Pm\text{-}3m$ Plastic phase	**390 → 280 K** **II** $Pbc2_1$	**280 → 3 K** **III** *Pbca*	**3 → 2 K** **IV** $P2_1'2_1'2_1$
$a_1\ a_1\ a_1$	$a_2\ b\ c$	$2a_2\ b\ c$	$2a_2\ b\ c$
non-Polar	Polar	non-Polar	
Paramagnetic			Ferrimagnetic

2. Experimental procedure

Synthesis

Anhydrous $FeCl_3$, quinuclidine hydrochloride, 2-propanol and 1-heptanol were purchased from commercial sources and used without any further purification.

In a glove-box, the quinuclidine hydrochloride (1 g, 6.77 mmol) was mixed with anhydrous $FeCl_3$ (1.01 g, 6.77 mmol) in a 8 mL vial. The mixture was heated at 150 °C during 12 h and the desired product was obtained as a pale orange powder. 2.0 g (100% yield). Single-crystals suitable for X-ray and neutron diffraction were grown by recrystallization of this compound in a mixture 2-propanol:1-heptanol (1:1). The solvent was allowed to slowly evaporate for 2 months. After this period, single-crystals suitable for X-ray and neutron diffraction were harvested. Elemental analysis: Found: C, 27.19; H, 4.21; N, 4.88; Fe, 17.93; Cl, 45.79%. Calcd. for $C_7H_{14}NFeCl_4$: C, 27.13; H, 4.55; N, 4.52; Fe, 18.02; Cl, 45.77%. Characteristic IR bands (cm^{-1}): 3204 (C–H), 2945 (C–H), 1461 (C–H sp^2), 1397 (C–H sp^2), 1036 (N–C), 961 (N–C3), 833 (N–C3), 613 (N–C2), 411 (N–C2), Characteristic Raman bands (cm^{-1}): 1367 (C–H sp^2), 1168 (C–H sp^3), 1120 (C–H sp^3), 1082 (N–C), 1020 (N–C), 858 (N–C3), 714 (C–C), 606 (N–C2), 374 (Fe–Cl), 330 (Fe–Cl), 138 (Fe–Cl), 106 (Fe–Cl) (see Fig. S1).

View Article Online
DOI: 10.1039/D0TC02341H

Physical Measurements of (quinuclidinium)[$FeCl_4$]

Single-crystal X-ray diffraction

The crystal structure of (quinuclidinium)[$FeCl_4$] was determined by single crystal X-ray diffraction at 300 and 100 K. Data were collected using Mo-Kα radiation (0.71073 Å) in an Agilent Technologies Supernova diffractometer. A single crystal of the compound with approximate dimensions 0.11 mm × 0.19 mm × 0.23 mm was employed. The data reduction was performed with the CrysAlis PRO program.[30] Data were corrected for Lorentz and polarization effects. All structures were solved by direct methods using the SIR92 program[31] and refined by full matrix least-squares on F^2 including all reflections (SHELXL97).[32] At 300 K, the quinuclidinium molecule is disordered in two position by means of a ca. 30 º rotation along the N1···C4 axis. The occupation factor of each part was refined leading to a ratio of 0.66:0.34. All non-hydrogen atoms were refined anisotropically, except those corresponding to disordered entities. H atoms were included at calculated positions and treated as riding atoms with isotropic thermal motion related to that of its parent atom. The final structure was refined as a two-component merohedral twin, implying that the compound crystallizes in a unit cell with a higher point group than that corresponding to the $Pbc2_1$ space group. The resolution in *Pbcm* space group yields greater R-factors and a highly organic cation with a tangled disorder that precludes to model it unambiguously. All the calculations for these structures were performed using the WINGX crystallographic software package.[33] The final structural parameters and figures of merit of the last refinements are summarized in Table S1 and the positional parameters are given the corresponding CIF files.

Single-crystal neutron diffraction

A suitable "neutron-sized" crystal with approximate dimensions of 2 × 2 × 2 mm^3 was mounted on a vanadium pin. The sample was placed on a close-circuit displex device on the monochromatic four-circle diffractometer D19 at ILL (Grenoble, France). The wavelengths used were 0.9455 Å and 1.4557 Å, provided by a flat Cu monochromator using the 331 and the 220 reflections, respectively, at $2\theta_M = 69.91°$ take-off angle. The sample was cooled down to 2 K and 10 K, with a ramp of 1 K/min cooling rate, and warmed up to 250 K and 295 K, with 2 K/min warming rate. The measurement strategy consisted on several omega (ω) scans with steps of 0.07° at different χ and φ positions.[34] These omega scans cover either 79° or 64° depending on the χ angle, in order to avoid collisions with the sample environment.

The NOMAD software from ILL was used for data collection. Unit cell determination was done by using PFIND and DIRAX programs, and processing of the raw data was applied using RETREAT and RAFD19 programs.[35-37] Absorption correction was applied using D19ABS program.[38]

The structure was refined by full matrix least-squares on F^2 including all reflections (SHELXL97).[32] For data collected at 250 and 10 K all atoms were refined anisotropically including the hydrogen atoms, which were located by Fourier difference. The disorder observed at 300 K on the X-ray measurements was used as starting point to refine the neutron data at this temperature. A similar disorder between two positons was included in the final model. However, the anisotropic thermal parameters of each quinuclidinium molecule was restrained to be equal using an EADP command in shelx. The only one component of this disorder was refined anisotropically. The H atoms were included at calculated positions and treated as riding atoms with isotropic thermal parameters restrained to be equal using an EADP command. All the calculations for these structures were performed using the WINGX crystallographic software package.[39] Table S2 gathers the crystal data and structure refinement parameters at 295, 250 and 10 K.

Thermal analysis

A Setaram calorimeter (DSC131) was used for the thermal analyses from 153 to 473 K under nitrogen atmosphere at a heating rate of 10 K/min. For this experiment, ca. 10 mg of sample were used and blank runs were performed.

Fourier transform infrared spectroscopy (FT-IR)

FT-IR measurements was performed on a Bruker Alpha Series FT-IR spectrometer equipped with an attenuated total reflectance (ATR) module. The ATR FT-IR spectra were recorded by collecting 24 scans of a compound in the ATR module.

Raman spectroscopy

The non-polarized Raman spectra of the sample was recorded in backscattering geometry with a Horiba T64000 triple spectrometer with the same protocol of reference.[40]

Variable temperature synchrotron X-Ray powder data collection

Synchrotron X-ray powder diffraction (SR-XRPD) measurements were performed at the high resolution station of the MSPD beamline (BL04) at ALBA synchrotron. The sample was introduced into a 0.7 mm glass capillary and measured in transmission at an energy of 22 keV (0.56376 Å wavelength determined from a Si NIST-640d reference) using the microstrip Mythen-II detector (six modules, 1280 channels/module, 50 μm/channel, sample-to-detector distance 550 mm). Temperature was controlled using an Oxford Cryosystems Series 700 Cryostream. Data from 1 to 43º (2θ) were collected during a 10 K/min ramp from 300 to 470 K every 30 s. The crystal structures were refined using Rietveld refinement with the FullProf suite program.[41]

Magnetization measurements

DC magnetic susceptibility measurements were performed using a Quantum Design PPMS magnetometer whilst heating from 2 to 300 K under different applied magnetic fields from 0.01 to 1 kOe. Magnetization as a function of field (H) was measured using the same magnetometer in the $-50 \leq H/\text{kOe} \leq 50$ at 2 K after cooling the sample in zero field.

Neutron powder diffraction

Neutron powder diffraction measurements were performed on D1B powder diffractometers at the Institute Laue-Langevin (ILL, Grenoble, France). Ca. 2 g of (quinuclidine)[$FeCl_4$] were used for the experiments, which were placed in a cylindrical vanadium container and held in a

DOI: 10.1039/D0TC02341H

liquid helium cryostat. High flux and medium resolution diffractometer D1B, operated at $\lambda = 2.525$ Å, was used to study the evolution of the sample in the low temperature range. Besides, high counting time neutron diffraction patterns were measured at 10 and 1.4 K in the angular range $5 \leq 2\theta \leq 128^{o}$. The collected data allowed us to solve and refine the magnetic structure.

Dielectric measurements

The complex dielectric permittivity ($\varepsilon_r = \varepsilon'_r - i\varepsilon''_r$) of cold-press pelletized samples was measured as a function of frequency and temperature building a parallel-plate capacitor coupled to a Solartron1260A Impedance/Gain-Phase Analyzer, capable to measure in the frequency range from 10 Hz up to 1 MHz using an amplitude of 1 V. The capacitor was mounted in a Janis SVT200T cryostat refrigerated, and with a Lakeshore 332 incorporated to control the temperature from 295 K up to 420 K. The data were collected on heating and before carrying out the measurement, the pellets were maintained at each temperature for two minutes to achieve thermal equilibrium.

Pelletized samples, with an area of approximately 13 mm^2 and a thickness of approximately 1 mm, were prepared by cold-press to fit into the capacitor. Gold was sputtered on the surfaces of the pelletized samples to ensure a good electrical contact.

All the dielectric measurements were carried out in a nitrogen atmosphere, performing several purging cycles with nitrogen gas to ensure that the sample chamber is completely free of atmospheric moisture.

3. Results and discussion

Crystal structures phase I to III

Along this section, the different structural phases observed on the (quinuclidinium)[FeCl$_4$] compound will be described. As defined by convention, the highest temperature solid phase is denoted as phase **I**, with subsequent lower temperature phases denoted as phase **II**, **III** and **IV** respectively.

Above 390 K, the phase **I** is observed in the SR-XRPD data (see Fig. 1). The crystal structure can be described in the cubic crystal system, with cell parameters $a = b = c = 7.1022(3)$ Å and a volume unit cell of 358.24(4) Å^3. The indexing of the synchrotron powder diffraction data suggests Pm-$3m$ as a possible space group. The best model corresponds with the organic cations placed on the corners of the unit cell, corresponding to the (0, 0, 0) and symmetry related positions, and the anions placed on the (0.5, 0.5, 0.5) position. The orientation of both cations and anions is highly disordered, which is in agreement with the isotropic character of the rotations described on plastic phases.[17-24] The free rotation of the quinuclidine molecule results in a centrosymmetric crystal structure. This behaviour is similar to the previously reported results for other quinuclidine-based compounds,[27-29] suggesting that quinuclidine-based hybrid complexes are promising to obtain plastic crystals.

View Article Online
DOI: 10.1039/D0TC02341H

The plastic phase was modelled using a series of spherical shells centred on the (0, 0, 0) and on the (0.5, 0.5, 0.5) positions for the organic cation and for the $[FeCl_4]$ unit, respectively. Due to the low number of observed reflections the symmetry adapted spherical harmonics was restrained to be an ideal sphere (see Fig. 1).

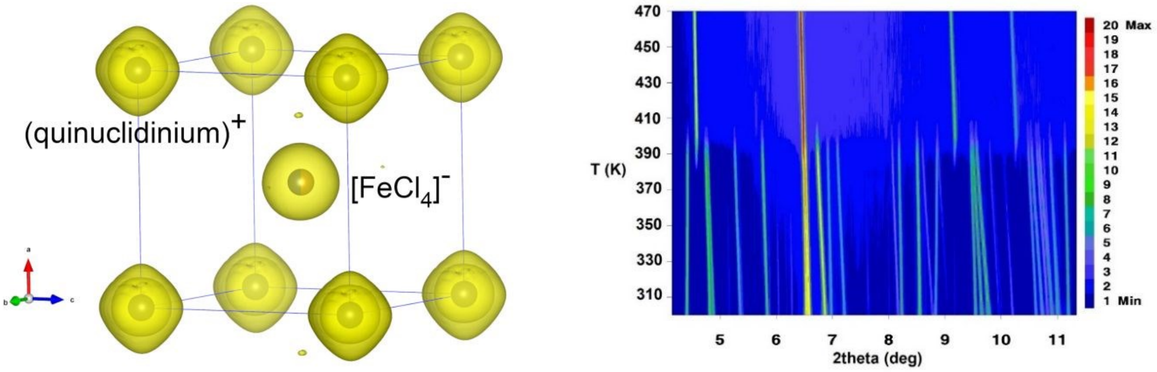

Fig. 1. (left) Calculated Fourier maps on the plastic phase derived from the refinement of the experimental data at 470 K (phase **I**, plastic phase) using the spherical shell refinement. (right) Temperature evolution of the synchrotron powder diffraction of the (quinuclidinium)$[FeCl_4]$ compound from RT to 470 K.

The density map around the $[FeCl_4]^-$ anions shows an almost spherical behaviour. However, the density map around the (quinuclidinium)$^+$ cation position presents octahedral shape (see Fig. 1). This indicates that the (quinuclidinium)$^+$ environment is not as isotropic as expected in a plastic crystal. However, the current data preclude a more sophisticated refinement using high order harmonics using the symmetry adapted spherical harmonics refinement to model the rotations present in the plastic phase. Nevertheless, this shape in the Fourier map could be due to a symmetry artefact, as the centre of mass of the quinuclidinium counter-ion is placed on the 1*a* Wyckoff position, which has octahedral (O_h) symmetry.

Below the plastic phase, the crystal structure can be described in the $Pbc2_1$ non-centrosymmetric orthorhombic space group with cell parameters $a = 6.71265(5)$ Å, $b = 13.26096(10)$ Å and $c = 14.64552(11)$ Å, obtained from the powder synchrotron X-ray data at RT. The nuclear phase transition from **I** to **II** is compatible with the signal observed on the DSC measurements at ca. 282 K (see Fig. S2 of electronic supplementary information; ESI). The asymmetric unit consists of a $[FeCl_4]^-$ anion and a quinuclidinium molecule to achieve electroneutrality. At RT, the organic cations are highly disordered. X-ray single crystal data collected at RT show a structure that can be modelled using two independent positions of the quinuclidinium molecule. Both molecules are quite close and the soft constrains are needed to refine the model. Neutron diffraction data collected in a larger single crystal at the same temperature show similar results. The observed Fourier map together with the structural model are shown in Fig. 2. The Fourier map suggests a non-negligible libration of the molecules at this temperature.

View Article Online
DOI: 10.1039/D0TC02341H

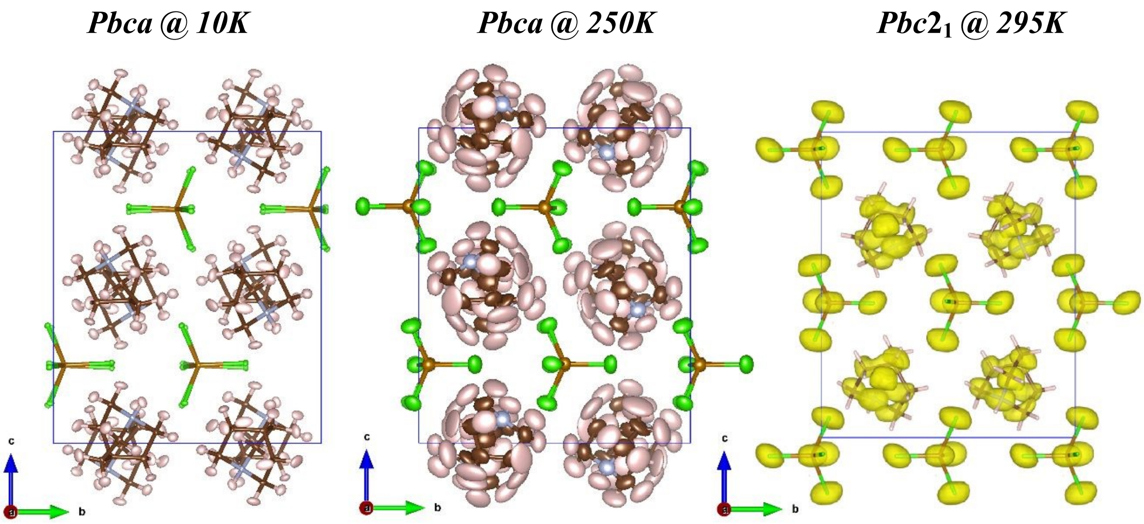

Fig. 2. view of the crystal structure along the *a*-axis at 10, 250 and 295 K. The displacement ellipsoids for 10 and 250 K are shown with 50% probability. At 295 K the observed Fourier map has been over-plotted to the structural model. For the sake of clarity, only one position of the disordered quinuclidinium molecules has been shown. Color codes: yellow, iron; green, chloride; brown, carbon; blue, nitrogen; pink, hydrogen.

The three-dimensional assembly can be described as a stacking of organic (quinuclidinium)$^+$ and inorganic $[FeCl_4]^-$ layers along the crystallographic *c*-axis (see Fig. 2). Each of these layers change of orientation following an ABCD stacking sequence (with A/C and B/D corresponding to the inorganic and organic layers, respectively). The crystal packing is sustained by an intricate network of electrostatic and non-covalent interactions that include hydrogen bonds and van der Waals forces. Based on the crystal structure, a net polarization is possible along the *c*-axis. However, due to the libration of the quinuclinide molecule, that is a cage-shape molecule with net dipole moment ($\mu = 3.1$ D calculated at the MP2/6-31 + G* level of theory),[27] the polarization signal can be significantly reduced.

Decreasing the temperature, reflections of the form (h+0.5, k, l) become to be illuminated (see detail on Fig. 3), that suggest a doubling of the *a*-axis with respect to the RT unit cell. Moreover, DSC measurements show a broad peak around 265 K. Nuclear structures at 250, 100 and 10 K, using both neutron and X-ray diffraction, suggest that the crystal structure can be solved in the *Pbca* centrosymmetric space group, with a doubling of the *a*-axis. The unit cell parameters refined at 10 K, $a = 13.0822(3)$ Å, $b = 12.5799(4)$ Å and $c = 14.6292(5)$ Å, suggest a more remarkable thermal contraction within the *ab*-planes than in the stacking direction along the *c*-axis.

The crystal structure of phase **III** is reminiscent of the one of phase **II**. The organic-inorganic layered structure pillared along the crystallographic *c*-axis is maintained in phase **III**.

View Article Online
DOI: 10.1039/D0TC02341H

Moreover, the libration of the quinuclidinium molecules is diminishing with the decreasing of the temperature. The doubling of the *a*-axis and the change of space group give rise to a blocking of the quinuclidinium molecules in two configurations that precludes the occurrence of a global polarization. The Rietveld refinements to phase **II** and **III** to the SR-XRPD at 300 and 100 K, respectively, as well as an overlapping of the crystal structure of both phases is shown in Fig. 3. The small peaks appearing in Fig. 3 which are not fitted by the model correspond to a non-identified second phase. The increasing of the temperature above RT produces the decreasing of this second phase. In the plastic phase, only those reflections corresponding with the indexed cubic unit cell are observed, and after decreasing again down to RT, the compound recrystallizes in to the RT phase (phase **II**) without any secondary phase. It deserves to be noted that the non-observation of the second phase reflections after the thermal treatment (see Fig. S3), suggests that these reflections can be due to a sub-product that crystallizes in the most stable phase after the recrystallization from the plastic phase.

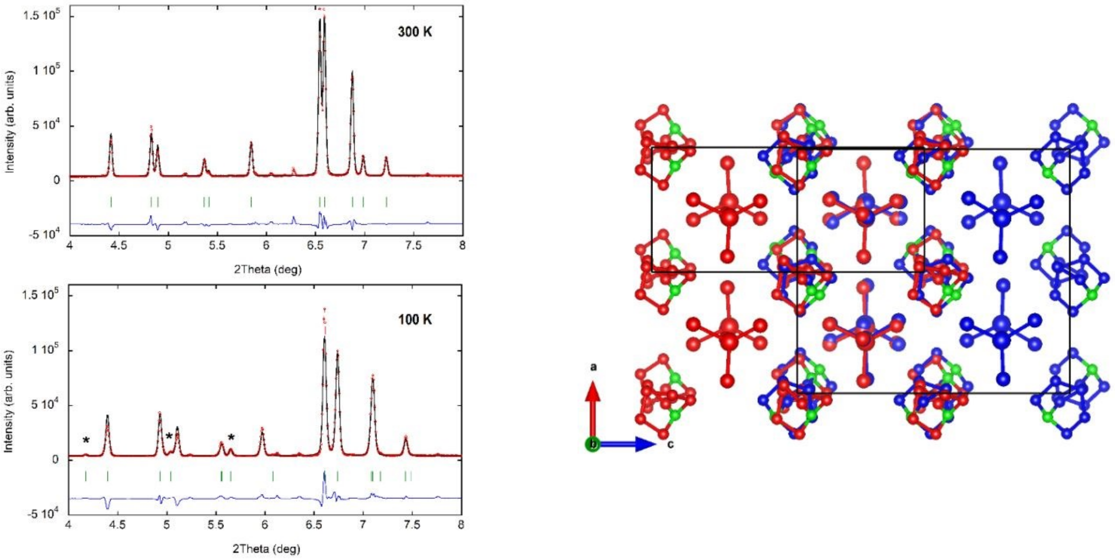

Fig. 3. (left) Rietveld refinement to the SR-XRPD data at 300 and 100 K to phase **II** and **III** (R_{Bragg}= 8.35 and 8.10), respectively. Observed and calculated patterns are represented by red points and by a solid black line, respectively. Positions of the Bragg reflections are represented by vertical green bars. The observed-calculated difference pattern is depicted as a blue line at the bottom of the figure. The asterisks mark the reflections which do not fit the structural model of RT. (Right): Unit cell of (quinuclidinium)$[FeCl_4]$ at 10 K (blue) and 295 K (red). The nitrogen atoms are shown in green and the hydrogen atoms have been omitted for the sake of clarity.

The crystallographic information, as well as the relevant distances at 10, 250 and 295 K, are presented in Tables S2 and S3-4, respectively. Fig. 2 shows the crystal structure of the title compound at three different temperatures, including the hydrogen atoms, where we have highlighted the importance of the molecular agitation using the observed Fourier map in the RT and 470 K refined structures.

View Article Online
DOI: 10.1039/D0TC02341H

Magnetometry measurements

Magnetic properties of the title compound were determined over the temperature range 2-300 K at different magnetic fields from 0.01 to 1 kOe in zero field cool (ZFC) and field cool (FC) mode. The magnetic susceptibility (χ_m) and the χ_mT versus T data at 1 kOe are plotted in Fig. 4.

χ_m displays perfect paramagnetic behavior above 10 K. The magnetic susceptibility data can be fitted to a Curie-Weiss law with paramagnetic Curie temperatures, θ_p, close to -1.4 K and an effective paramagnetic moment μ_{eff} = 6.06(1) μ_B per Fe ion; which is slightly higher than the expected one for high spin d^5 Fe(III) ions (μ_{eff} = 5.92 μ_B per Fe ion) but is in a good agreement with those found in other halometallate compounds based on $[FeCl_4]^-$ ions.[42-43] At room temperature, the χ_mT value of 4.49 emu K mol^{-1} Oe^{-1} agrees well with the expected one (4.38 emu K mol^{-1} Oe^{-1} for Fe(III) ions with a magnetic spin S = 5/2). This value remains almost constant down to 20 K, where it begins to fall due to the magnetic interactions between Fe(III) ions. The negative θ_p value together with the reduction of the χ_mT with decreasing temperature suggest antiferromagnetic behavior. Moreover, below 4 K, the ZFC-FC molar susceptibility measured under 1 kOe displays an inflexion point near 3 K (see inset of Fig. 4, left), suggesting the existence of long-range magnetic order. When the magnetic field is decreasing, this magnetic signal increases in value and starts to split. This feature is characteristic of a ferromagnetic component in its magnetic structure.

In order to study the response of the magnetization with the applied magnetic field, we have measured the M(H) curves within ± 50 kOe at 2 K (Fig. 4). The M(H) loop displays a saturating value of 4.9 μ_B per Fe ion, which agrees with the expected fully-saturated value of 5 μ_B per atom for Fe(III) ion. In addition, a small hysteresis loop is found (H_C = 52 Oe, Mr = 0.05 μ_B, see the inset in Fig. 4, right), as expected from the splitting of the M_{ZFC}(T) and M_{FCW}(T) curves below to T = 3 K. In overall, we can conclude that (quinuclidinium)[$FeCl_4$] shows an antiferromagnetic behavior with the presence of a ferromagnetic component, which is characteristic of a ferrimagnetic behavior due to the non-compensation of the magnetic moments or an spin-canting.

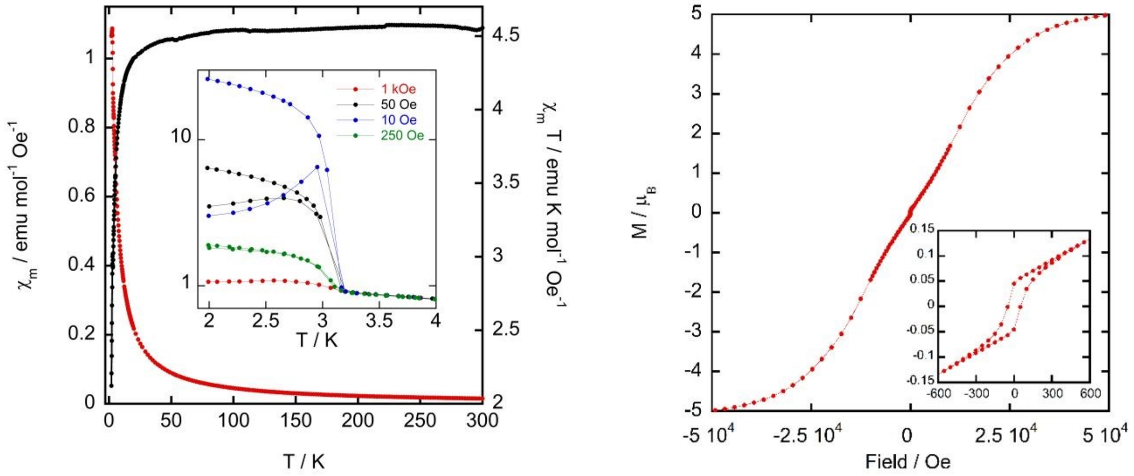

View Article Online
DOI: 10.1039/D0TC02341H

Fig. 4. (left) magnetic susceptibility (χ_m) and the χ_mT versus T at 1 kOe. The inset show the ZFC-FC measurements at different magnetic fields from 0.01 to 1 kOe. (Right): Magnetization measurements at 2 K. The inset show and enlargement of the low magnetic field region.

Magnetic structure phase IV

The existence of long range magnetic order was confirmed using neutron powder diffraction. Two high-flux neutron patterns were collected at the paramagnetic phase (10 K) and at the ordered phase (1.4 K) on the high flux D1B diffractometer, operated with a wavelength of $\lambda = 2.52$ Å. A comparative view of both patterns reveals the presence of a new sharp Bragg peak and magnetic contributions on top of some of the structural peaks (see Fig. S3 of ESI). This is a direct evidence of the long magnetic order below T_c, in good agreement with the results obtained from the magnetometry measurements (*see magnetic properties section*). Due to the weak magnetic signal, the overlap between nuclear reflections and the considerable background, the nuclear contribution has been subtracted from the pattern at 1.4 K (by subtracting the intensity of the pattern at 10 K). Both diffraction patterns were normalized to the same monitor in order to obtain the best difference pattern. The difference pattern isolates the magnetic contribution and, therefore, a more accurate refinement of the magnetic structure can be undertaken. To complete this study and to have an idea of the possible magneto-structural correlation, a complete data set using single crystal diffraction was collected on D19 with a wavelength of 1.4557 Å. Although this wavelength is relatively long, the integration of some magnetic low Q-reflections was not possible. Moreover, the base temperature on the D19 self-dedicate displex is ca. 2 K, which is slightly above the temperature collected on D1B. As we will discuss later on, that will play an important role in this compound, with a 3D magnetic ordering close to 3 K (see Fig. S4).

The magnetic reflections observed on the difference pattern can be indexed with the $\mathbf{k} = (0, 0, 0)$ propagation vector. Symmetry analysis using the Bertaut's symmetry analysis method,[44] employing the BCS k-Subgroupsmag utility[45] and BasIreps program,[46] shows eight different irreducible representations (irreps) compatible with the propagation vector and with the crystal structure solved at 10 K. Nevertheless, neither of these eight potential maximal magnetic space groups fit properly the experimental data. In order to fit the data, different subgroups were tried by a simulated annealing procedure. The best model was obtained combining two of the previous irreps, $m\Gamma_2^+$ ($Pb'c'a.a,b,c;0,0,0$) and $m\Gamma_2^-$ ($Pb'ca.-c,-a,b;0,0,0$), written following the notation of the BCS. The linear combination of these two irreps drives to $P2_1'2_1'2_1$ Shubnikov space group, which is a sub-group of the parent *Pbca*. The simulated annealing refinement with the D1B data and the least square refinement of the obtained model on D1B against the D19 data are shown in Fig. 5.

The breaking of symmetry from *Pbca* parent space group to the $P2_1'2_1'2_1$ Shubnikov space group produces a splitting in the orbits of the magnetic atoms. Along these refinements, the modulus of the magnetic moments of both iron sites were forced to be equal. This assumption is reasonable as both irons have equivalent environments, even if it could be refined independently in the $P2_1'2_1'2_1$ subgroup. The value of the magnetic moment obtained with the

D1B data was 4.81(3) μ_B, which is not far away from the expected value for a Fe^{3+} (S = 5/2). However, for the D19 data, where the structural and magnetic structure were refined simultaneously, the obtained value was 3.7(2) μ_B. This difference can be explained by the increase of the collecting temperature on the D19 (ca. 2 K), and the fact that we were measuring very close to the ordering temperature (3 K) and therefore the magnetic moments are not completely saturated.

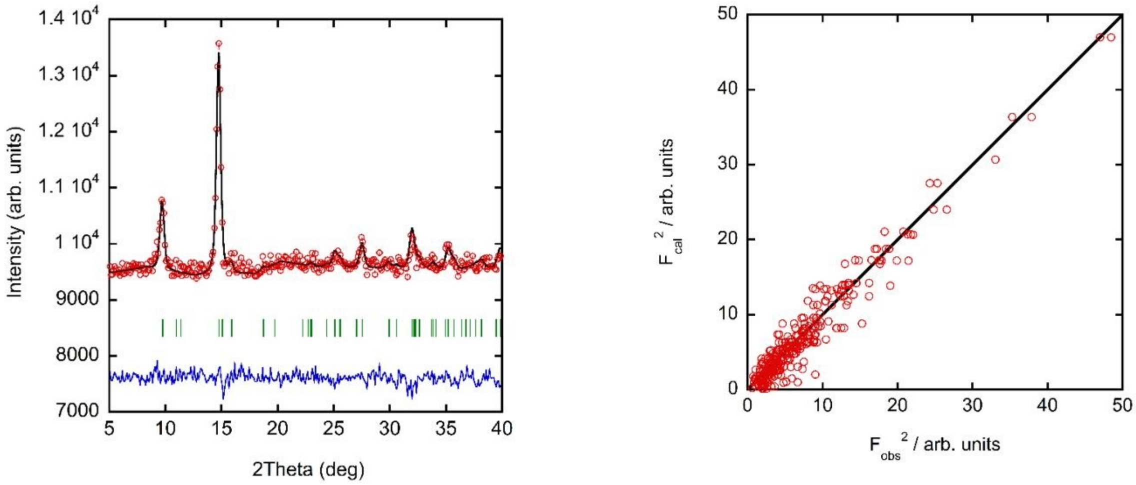

Fig. 5. (Left) Experimental (red circles) neutron diffraction data and Simulated Annealing fit (black solid line) to the difference pattern between 1.5 and 10 K on D1B. The difference between the experimental data and the fit is represented as a solid blue line; the markers (green vertical lines) indicates the position of the magnetic Bragg reflections. (Right) Plot of the observed *vs*. calculated squared magnetic structure factors (resulted from Rietveld refinement) collected at 2 K at the D19 instrument. The experimental data are represented as red circles and the ideal case ($F_{cal}^2 = F_{obs}^2$) is represented as a solid black line.

The magnetic structure can be described as non-compensate antiferromagnetic zig-zag chains along the *c*-direction. The antiferromagnetic coupling takes place along Fe-Cl···Cl-Fe direction. The shortest distance between the two adjacent chloride atoms along the *c*-direction is 3.84 Å and the Fe-Cl···Cl-Fe torsion angle is ca. 173°. The shortest Cl···Cl distance (ca. 3.72 Å) occurs between $FeCl_4$ tetrahedral units along the *b*-axis, these adjacent tetrahedral units are packed with a slightly off sigma-holes between each other. Along this direction, the magnetic moments are coupled ferromagnetically. It deserves to be noted that the shortest Fe···Fe distance (6.3428 Å) is along the *b*-axis due to the sigma-hole crystal packing. As the Cl···Cl distances are longer than the standard van der Waals radius, it is not certain that the Cl···Cl interaction plays a principal role in the long-range magnetic order. Nevertheless, dipolar interaction can couple the ferromagnetic chains (which run along the *b*-axis) antiferromagnetically with the adjacent chains (along *a*- and *c*-axis). Similar magnetic structures have been reported by other tetraferrate compounds.[41,47]

It deserves to be noted that, although this model is mainly antiferomagnetic by symmetry, a net component of the magnetic moment along the *c*-axis is allowed. This ferromagnetic component is produced due to the non-compensation of the magnetic moments in the *ab*-plane. The small tilt of the magnetic moment out of the plane should be in the origin of the weak ferromagnetic signal observed on the macroscopic magnetometry measurements. The estimation of the

View Article Online
DOI: 10.1039/D0TC02341H

ferromagnetic component based on the magnetometry measurements is about 0.05 μ_B per Fe^{3+} atom (0.2 μ_B per unit cell); value that is below the precision of our neutron diffraction studies. However, in order to provide a complete magnetic model, this component has been included and fixed in the last refinement. As expected no change in the refined statistics was observed. A detailed view of the refined magnetic structure has been shown in Fig. 6, were the canting contribution has been multiplied by a factor 10 (0.5 μ_B per Fe^{3+} atom) for the sake of visual clarity.

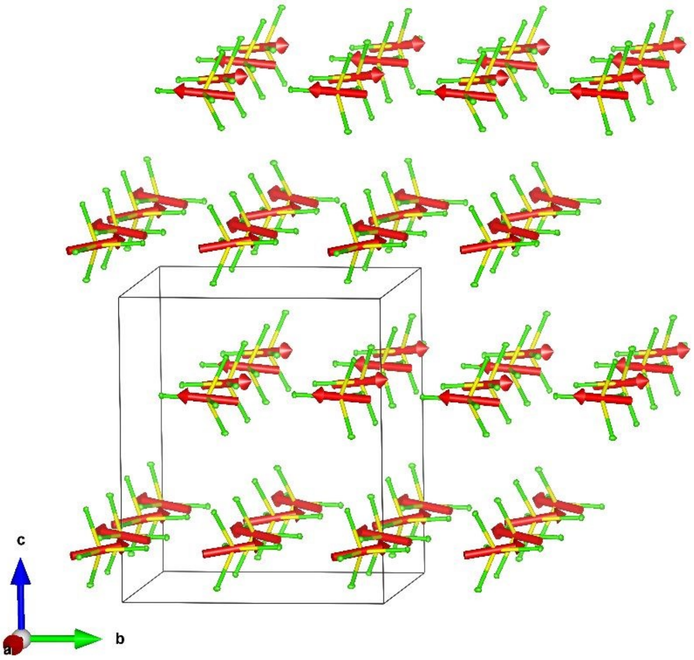

Fig. 6. Magnetic structure of (quinuclidinium)[$FeCl_4$] at 1.8 K. Color codes: yellow, iron; green, chloride; red, magnetic spin. The organic cations have been omitted for the sake of clarity

Dielectric measurements:

The dielectric constants of a polycrystalline pellet were measured as a function of the temperature at frequencies from 1 to 10 kHz. The real part of the complex dielectric permittivity collected on a pressed sample of (quinuclidinium)[$FeCl_4$] shows a continuous increase from RT to 370-380 K, with a slight dependence with the frequency (Fig. 7). Above this temperature, a sharp phase transition, that is characteristic of ferroelectric/paraelectric phase transitions,[27] is observed. Unfortunately, this ferroelectric/paraelectric phase transition occurs close to the temperature limit of our experimental set-up and the paralectric phase cannot be fitted using a Curie-Weiss law. However, this abrupt increase in the dielectric permittivity is compatible with the observed signals in the DSC measurements and the transformation from phase **II** to phase **I** observed on the powder synchrotron X-ray data (see Fig. 1 and S1). The value of the permittivity increases drastically with the increase of the temperature, reaching a maxima of 10^5 at 420 K (measured at 1 kHz). This value is giant in comparison with similar compounds previously reported in the bibliography, which is the main feature of the ferroelectric transition.[27, 28. 47, 48].

View Article Online
DOI: 10.1039/D0TC02341H

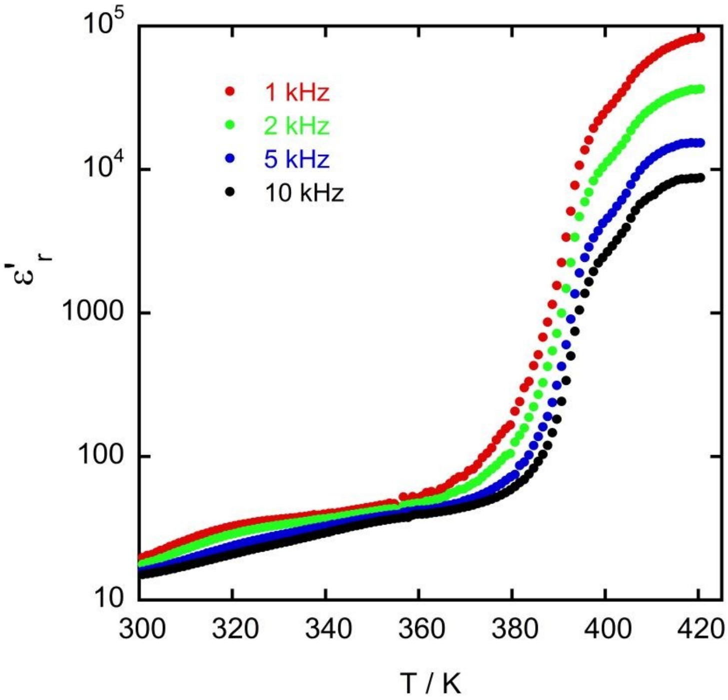

Fig. 7. Relative permittivity as a function of temperature for different frequencies, in the range 300-420 K. The measurements were taken applying an amplitude of 1 V to cold-press pelletized samples.

Usually when freezing, the dielectric constant of a substance falls markedly but, with many plastic crystals, the dielectric constant continues to rise on lowering the temperature, the curve for the plastic state being almost continuous with the curve for the liquid, and falling sharply only at the transition point. Two anomalies at 390 and 410 K are observed on all the frequencies. In this temperature range both phases, **I** and **II**, coexist. Therefore, the dynamic balance between both phases is expected. The onset of molecular reorientation and the later isotropic reorientation of the polar cations can be at the origin of these anomalies. The saturation values of the ε′ are observed for all explored frequencies at temperatures slightly above 410 K. However, no sign of decrease of ε′ with the later increase on the temperature has been observed up to the maximum temperature of 420 K. This broad signal suggests an intricate dynamical behavior in the plastic phase. This behavior could be of interest for electrochemical applications.

4. Conclusions

The experimental results have demonstrated the occurrence of four different phases on the (quinuclidinium)[$FeCl_4$] compound. The complete phase diagram involves a phase transition between paraelectric-to-polar phase at 390 K, from polar phase-to-antiferroelectric around 280K and from paramagnetic-to-antiferromagnetic at 3.5 K. Above RT, the occurrence of paraelectric-to-polar phase transition involves a plastic phase with a giant increase in the real part of the dielectric permittivity. The hybrid organic-inorganic compounds combining plastic

View Article Online
DOI: 10.1039/D0TC02341H

phases with polar phases at room temperature are particularly desirable, as these could present small coercive electric field, allowing switchable polarization with relative low voltages and high-frequency performance. Moreover, the occurrence of plastic phases in this kind of systems has been correlated to an increase of the ionic conductivity, which could be of interest for further applications.

The polar phase is stable between 390 and 280 K. Below this temperature, a second phase transition involving the doubling of the unit cell along the *a*-axis was observed. The suppression of the polarization is due to the strict compensation of the electric dipoles because of the occurrence of a centrosymmetric space group. A new breaking of symmetry was needed to obtain a magnetic model below 3.5 K. The phase **IV** gives rise to a globally antiferromagnetic structure with the antiferromagnetic moments non-compensated along the *c*-axis. This magnetic structure is compatible with the weak-ferromagnetic signal observed in the magnetometry measurements.

ASSOCIATED CONTENT

*ELECTRONIC SUPLEMENTARY INFORMATION

† Electronic supplementary information (ESI) available: Crystallographic information, CIF data, details on the thermal analysis, neutron diffraction experiments, single-crystal X-ray diffraction analysis, ionic conductivity and variable-temperature synchrotron X-ray powder diffraction analysis. CCDC 2003976-2003980. For ESI and crystallographic data in CIF or another electronic format see DOI: XXXX

AUTHOR INFORMATION

Corresponding Authors

*E-mail for P. G-I: gonzalez-izquierdo@ill.fr

*E-mail for O.F.: fabelo@ill.fr

*E-mail for I.d.P: depedrovm@unican.es

ORCID

Oscar Fabelo: 0000-0001-6452-8830
Imanol de Pedro: 0000-0002-5581-2220
Manuel Sánchez-Andújar: 0000-0002-3441-0994
Garikoitz Beobide : 0000-0002-6262-6506
Oriol Valcorba: 0000-0001-6499-7688
Laura Canadillas-Delgado: 0000-0001-8679-5008

View Article Online
DOI: 10.1039/D0TC02341H

CONFLICTS OF INTEREST

There are no conflicts of interest to declare.

ACKNOWLEDGMENTS

Financial support from Universidad de Cantabria (Proyecto Puente convocatoria 2018 funded by SODERCAN_FEDER), Universidad del País Vasco/Euskal Herriko Unibertsitatea (GIU17/50 and PPG17/37) and Ministerio de Economia y Competividad (MAT2017-89239-C2-(1,2)-P, MAT2017-83631-C3-3-R and MAT2017-86453-R). The authors gratefully acknowledge Technical and human support provided by SGIKer (UPV/EHU, MINECO, GV/EJ, ERDF, and ESF). The paper is (partly) based on the results of experiments carried out at the ALBA Synchrotron Light Source in Barcelona and Institute Laue-Langevin (ILL) of Grenoble (Proposals 5-31-2580 and 5-31-2460).

TOC

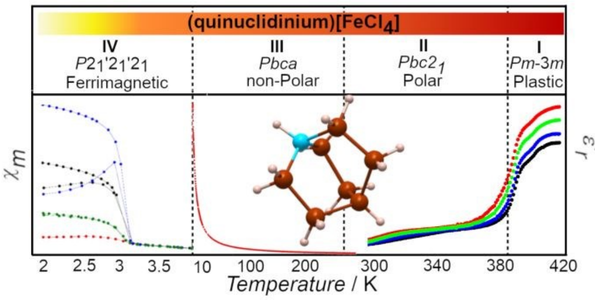

REFERENCES

[1] A. Kojima, K. Teshima, Y. Shirai and T. Miyasaka. *J. Am. Chem. Soc.,* 2009, **131**, 6050-6051.

[2] D. Luo, W. Yang, Z. Wang, A. Sadhanala, Q. Hu, R. Su, R. Shivanna, G. F. Trindade, J. F. Watts, Z. Xu, T. Liu, K. Chen, F. Ye, P. Wu, L. Zhao, J. Wu, Y. Tu, Y. Zhang, X. Yang, W. Zhang, R. H. Friend, Q. Gong, H. J. Snaith and R Zhu. *Science*, 2018, **360**, 1442-1446.

[3] J. urschka, N. Pellet, S. J. Moon, R. Humphry-Baker, P. Gao, M. K. Nazeeruddin, and M. Grätzel. *Nature,* 2013, **499**, 316-319.

[4] B. Saparov, and D. B. Mitzi. *Chem. Rev.,* 2016, **116**, 4558-4596.

[5] N. J. Jeon, J. H. Noh, W. S. Yang, Y. C. Kim, S. Ryu, J. Seo and S. I. Seok. *Nature,* 2015, **517**, 476-480.

[6] S. Han, X. Liu, Y. Liu, Z. Xu, Y. Li, M. Hong, J. Luo and Z. Sun. *J. Am. Chem. Soc.,* 2019, **141**, 12470-12474.

[7] S. Wang, X. Liu, J. Li, C. Ji, Z. Sun, Z. Wu, M. Hong and J. Luo. *J. Am. Chem. Soc.,* 2019, **141**, 7693-7697.

[8] M. Patel, K. G. Chandrappa and A. J. Bhattacharyya. *Electrochim. Acta*, 2008, **54**, 209-215.

DOI: 10.1039/D0TC02341H

[9] M. Yamada, M. Kondo, J. Mamiya, Y. Yu, M. Kinoshita, C. J. Barrett and T. Ikeda. *Angew. Chem. Int. Ed.,* 2008, **47**, 4986 –4988.

[10] D. R. MacFarlane and M. Forsyth. Adv. Mater., 2001, **13**, 957-966.

[11] J. M. Pringle, P. C. Howlett, D. R. MacFarlane and M. Forsyth. *J. Mater. Chem.,* 2010, **20**, 2056–2062.

[12] M. Forsyth, P. Meakin, D. R. MacFarlane and A. J. Hill. *J. Phys.: Condens. Matter,* 1995, **7**, 7601.

[13] D. R. MacFarlane, J. Sun, P. Meakin, P. Fasoulopoulos, J. Hey and M. Forsyth. *Electrochim. Acta,* 1995, **40**, 2131-2136.

[14] H. Aono, E. Sugimoto, Y. Sadaoka, N. Imanaka, and G. Y. Adachi. *Solid State Ion.,* 1990, **40**, 38-42.

[15] D. H. Kothari, D.K. Kanchan and P. Sharma. *Ionics,* 2014, **20,** 1385–1390.

[16] J. Timmermans. *J. Phys.Chem. Solids*. 1961, **18**, 1−8.

[17] R. Brand, P. Lunkenheimerand A. Loidl. *J. Chem. Phys.,* 2002, **116**, 10386−10401.

[18] N. Hoshino, T. Takeda, and T. Akutagawa. *RSC Adv.,* 2014, **4**, 743−747.

[19] Y. Z. Sun, B. Huang, W. J.; Xu, D. D. Zhou, S. L. Chen, S. Y. Zhang, Z. Y. Du, Y. R. Xie, C. T. He, W. X. Zhang and X. M. Chen. *Inorg. Chem,* 2016, **55**, 11418−11425.

[20] M. Matsuki, T. Yamada, N. Yasuda, S. Dekura, H. Kitagawa and N. Kimizuka. *J. Am. Chem. Soc.*, 2018, **140**, 291−297.

[21] J. Salgado-Beceiro, S. Castro-García, M. Sánchez-Andújar and F. Rivadulla. *J. Phys. Chem. C*, 2018, **122**, 27769-27774.

[22] J. N. Sherwood. The Plastically Crystalline State: Orientationally Disordered Crystals; Wiley: Chichester, New York, 1979.

[23] D. MacFarlane, J. Huang and M. Forsyth. *Nature* 1999, **402**, 792 –794.

[24] J. Sun, D. MacFarlane and M. Forsyth. Solid State Ion. 2002, **148**, 145–151.

[26] Y.Abu-Lebdeh, P. J. Alarco, and M. Armand. *Angew. Chem. Int. Ed.* 2003, *42*, 4499 –4501

[27] J. Harada, T. Shimojo, H. Oyamaguchi, H.Hasegawa, Y. Takahashi, K. Satomi, Y. Suzuki, J. Kawamata and T. Inabe. *Nat. Chem.,* 2016, **8**, 946-952

[28] Y. M. You, Y.Y. Tang, P. F. Li, H. Y. Zhang, W. Y. Zhang, Y. Zhang, H. Y. Ye, T. Nakamura, and R. G. Xiong. *Nat. Commun*., 2017, **8**, 14934.

[29] J. Harada, Y. Kawamura, Y. Takahashi, Y. Uemura, T. Hasegawa, H. Taniguchi and K. Maruyama. *J. Am. Chem. Soc.,* 2019, **141**, 9349−9357.

[30] Agilent. *CrysAlis PRO* Agilent Technologies Ltd, Yarnton, England, 2010.

[31] A. Altomare, G. Cascarano, C, Giacovazzo and A. Guagliardi. *J. Appl. Crys.,* 1993, **26**, 343-350.

[32] G. M. Sheldrick. *Acta Crys.* 2008, **A64**, 112-122.

[33] L. J. Farrugia. *J. Appl.Cryst.* 1999, **32**, 837-838.

[34] P. González-Izquierdo, M. T. Fernández-Díaz, O. Fabelo, I. de Pedro and L. Cañadillas Delgado. Crystal structure determination of the (trimim)[$FeBr_4$] hybrid halometallate compound; Institut Laue-Langevin (ILL): Grenoble, 2019; DOI: 10.5291/ILL-DATA.5-12-341.

[35] A. J. M. Duisenberg. *J. Appl. Cryst,* 1992*,* **25**, 92-96

[36] G. J. McIntyre and R. F. D. Stansfield. *Acta Cryst.,* 1988*,* **A44***,* 257-262.

View Article Online
DOI: 10.1039/D0TC02341H

[37] C. Wilkinson, H.W. Khamis, R. F. D. Stansfield and G. J. McIntyre. *J. Appl. Crystallogr.*, 1988, **21**, 471-478.

[38] J. C. Matthewman, P. Thompson and P. J. Brown. *J. Appl. Crystallogr.,* 1982, **15**, 167-173

[39] L. J. Farrugia. *J. Appl.Cryst.* 1999, **32**, 837-838.

[40] A. García-Saiz, I., de Pedro, O. Vallcorba, P. Migowski, I. Hernández, L. F. Barquin, I. Abrahams, M. Motevalli, J. Dupont, J. A. Gonzalez and J. R. Fernández. *RSC Adv.*, 2015, **5**, 60835-60848

[41] J. Rodríguez-Carvajal. *Physica B: Condens. Matt.,* 1993, **192**, 55–69.

[42] A. García-Saiz, P. Migowski, O. Vallcorba, J. Junquera, J. A. Blanco, J. A. González, M. T. Fernández-Díaz, J. Rius, J. Dupont, J. R. Fernández and I. de Pedro. *Chem. Eur. J.*, 2014, **20**, 72-76.

[43] P. González-Izquierdo, O. Fabelo, G. Beobide, I. Cano, I. R de Larramendi, O. Vallcorba, J. R. Fernández, M. T. Fernández-Díaz, I. de Pedro. *RSC Adv.*, 2020, **10**, 11200-11209.

[44] E. Bertaut. *Acta Crystallogr. A,* 1968, **24**, 217–231.

[45] M. Perez-Mato, S.V. Gallego, E.S. Tasci, L. Elcoro, G. de la Flor, and M.I. Aroyo. Annu. Rev. Mater. Res., 2015, **45**, 13.1-13.32

[46] J. Rodriguez-Carvajal, BASIREPS: A program for calculating irreducible representations of space groups and basis functions for axial and polar vector properties. (See ftp://ftp.cea.fr/pub/llb/divers/BasIreps).

[47] G.-M. Fan, J.-X Gao, C. Shi, H. Yu, L. Ye, J.-Y. Jiang, C. Shuai, Y. Zhang and H.-Y. Ye. *CrystEngComm.*, 2018, **20**, 7058-7061.

[48] Y. B.Tong, Z. F. Tian, H. B. Duan, Z. P. Zhu, T. Y. Hong, S. P. Zhao and J. K. Yang *Chem. Asian J.,* 2019, **14**, 582 –591